

Article

Fabrication of Micron-Structured Heatable Graphene Hydrophobic Surfaces for Deicing and Anti-Icing by Laser Direct Writing

Shichen Li ^{1,†}, Mian Zhong ^{1,2,*,†}, Yao Zou ¹, Man Xu ³, Xinyi Liu ³, Xiaoqing Xing ¹, Huazhong Zhang ¹, Yong Jiang ³, Chao Qiu ⁴, Wenfeng Qin ⁴, Meng Li ⁴, Qiang He ^{5,*} and Chao Zhou ^{1,2}

¹ Institute of Electronic and Electrical Engineering, Civil Aviation Flight University of China, Guanghan, Deyang 618307, China; lscxy19990217@163.com (S.L.); zouyao670427@163.com (Y.Z.); tezrj.love@163.com (X.X.); zhz_233@yeah.net (H.Z.); zc_cafuc@163.com (C.Z.)

² Institute of Civil Aviation Intelligent Sensing and Advanced Detection Technology, Civil Aviation Flight University of China, Guanghan, Deyang 618307, China

³ School of Mathematics and Physics, Southwest University of Science and Technology, Mianyang 621010, China; 15237213981@163.com (M.X.); lxy_shea@163.com (X.L.); y_jiang@swust.edu.cn (Y.J.)

⁴ College of Aviation Engineering, Civil Aviation Flight University of China, Guanghan, Deyang 618307, China; chaoqiu1987@163.com (C.Q.); qwfgrh@126.com (W.Q.); mokechi@163.com (M.L.)

⁵ College of Civil Aviation Safety Engineering, Civil Aviation Flight University of China, Guanghan, Deyang 618307, China

* Correspondence: mianzhong@cafuc.edu.cn (M.Z.); hq@cafuc.edu.cn (Q.H.)

† These authors contributed equally to this work.

Abstract: As a novel method to prepare graphene, the laser-induced graphene (LIG) technology has numerous outstanding properties and has been widely applied in various fields. Nevertheless, the challenge remains to easily and efficiently prepare multifunctional surfaces of graphene through laser microregulation and fine structure design. Here, we successfully fabricated a micron-structure gully graphene surface with hydrophobicity and electrothermal functionality under atmospheric conditions using a 10.6 μm CO₂ laser to directly write on the surface of a polyimide film (PI). The impact of the laser scanning speed on the surface morphology and chemical composition of the product was investigated by analyzing the SEM (scanning electron microscope) observations and Raman spectra, respectively. The mechanical stability of the surface was studied by analyzing the contact angle of water droplets on the surface after mechanical circulation and the delayed icing effect after repeated icing. The deicing and anti-icing performance of the surface were analyzed based on its resistance to surface icing and electric deicing time. According to the experimental results, we first observed a linear negative correlation between the generated structure linewidth and the laser scanning speed. Additionally, we successfully achieved one-step preparation of primitive continuous graphene structures with a superhydrophobic capability (151°). Furthermore, our findings indicate that micron-structured graphene surfaces exhibit excellent mechanical stability, effectively delay icing formation, and demonstrate efficient electric deicing effects. These results demonstrate the potential application of CO₂ laser-induced graphene technology in the field of surface preparation for deicing and anti-icing. This work offers a novel one-step approach for the fabrication of micron-structured heatable graphene surfaces with simultaneous superhydrophobicity, deicing, and anti-icing functionalities on polymer substrates.

Keywords: CO₂ laser direct-writing; polyimide film; hydrophobic surface; deicing and anti-icing



Citation: Li, S.; Zhong, M.; Zou, Y.; Xu, M.; Liu, X.; Xing, X.; Zhang, H.; Jiang, Y.; Qiu, C.; Qin, W.; et al.

Fabrication of Micron-Structured Heatable Graphene Hydrophobic Surfaces for Deicing and Anti-Icing by Laser Direct Writing. *Coatings* **2023**, *13*, 1559. <https://doi.org/10.3390/coatings13091559>

Academic Editors: Eric Loth and Joachim Albrecht

Received: 30 June 2023

Revised: 31 August 2023

Accepted: 1 September 2023

Published: 6 September 2023



Copyright: © 2023 by the authors. Licensee MDPI, Basel, Switzerland. This article is an open access article distributed under the terms and conditions of the Creative Commons Attribution (CC BY) license (<https://creativecommons.org/licenses/by/4.0/>).

1. Introduction

Graphene is widely used in physics, materials, optics, chemistry, electronics, and medicine due to its excellent properties of high flexibility, high thermal conductivity, high electrical conductivity, and optical response. Numerous research teams have developed sensor devices [1,2], transistors [3], new energy batteries [4], desalination filters [5,6], energy

storage [7,8], flexible displays [9], microfluid systems [10], actuators [11–13], and deicing devices [14,15]. Currently, graphene can be obtained via mechanical exfoliation [16], vapor deposition [17], redox [18], SiC epitaxial growth [19], and laser induction [20]. Among them, laser-induced graphene (LIG) was first proposed in 2014, and Tour et al. used CO₂ laser direct writing on a polyimide (PI) surface to transform it into a 3D porous graphene surface. This new technology has high precision, flexibility, and good structure, and has garnered the attention of many research teams. Many types of lasers are increasingly used in this field, such as near-infrared lasers [21,22] and ultraviolet lasers [23,24]. Meanwhile, graphene precursor substrate materials have been expanded from various carbon-rich polymers to carbon-containing materials such as wood [25], coconut shells, bread, fabrics [26], and leaves [27]. LIG technology has been used to develop sensors [28], antibacterial and antiviral materials [29], RF heaters [30], high-performance microcapacitors [31], multishape flexible heating films [32], and aircraft deicing applications [33,34].

Considering the minimal thermal impact of the laser technology, high-precision processing, noncontact processing, simple repeatability, and numerous advantages of graphene, several research teams have conducted studies on producing nanostructured graphene surfaces with specific structures such as flower patterns. For example, the femtosecond-laser irradiation of graphene films immersed in distilled water was used to prepare graphene microflower surfaces with special nanostructured edges [35]. N-doped graphene was selectively patterned for ablation to obtain topologies for charge carrier measurements [36]. However, the laser in this part of the study only served as an auxiliary processing tool following the graphene production. LIG exhibits similar characteristics to graphene, where patterns and structures are simultaneously formed during the laser beam movement. Therefore, the microregulation of the laser and fine design to prepare patterned graphene surfaces is a more noteworthy approach.

Laser parameters, including power, spot size and scanning speed, are the primary factors that affect the laser processing effect. Microregulation aims to achieve the differential laser processing effects by adjusting the laser parameters. In recent years, many teams have accumulated some foundation in this direction. The Tour's team of LIG technology has systematically explored the influence of different laser irradiation energy [37] and defocusing amount [38] on the morphology and the hydrophobic properties of graphene and the preparation atmosphere [39]. Subsequent research teams have also explored methods based on Joule heat [40] and secondary laser processing [41] to improve the quality of graphene generation. Based on the advantages of laser processing to achieve fine design of patterns, using lasers in the wavelength range of 355 nm–10.6 μm, the graphene surface with super hydrophobic properties can be easily and quickly prepared by introducing fluorine functional groups [42], adjusting laser power [43], changing scanning speed [44], adjusting the control point per inch (DPI) parameter [45], bionic patterning design [46], and constructing the Janus structure [47]. These surfaces exhibit more stable superhydrophobic desalination and Joule thermal properties than traditional materials, and have better deicing potential than fluororubbers, with complex preparation steps [48–51]. The graphene surface with micro- and nanostructures is a new type of hydrophobic, deicing and anti-icing material; however its low- and high-temperature resistance, hydrophobic stability, and graphene adhesion have always been the main factors that limit its development. At present, the key relationship between the most common CO₂ laser parameters and microregulation in the preparation of superhydrophobic LIG surfaces have not been fully explored. The research on the microstructure stability, Joule heat, and superhydrophobic properties caused by scanning speed is relatively lacking.

In this work, the patterning design of a micron-structure graphene surface was first performed on the surface of PI based on the LIG technology regulation, and a micron-structure gully graphene surface was obtained. Then, scanning electron microscopy (SEM) was used to observe the effects of the scanning speed on the surface morphology of graphene and contact angle of water droplets (the surface prepared at 50–125 mm/s). The delayed icing effect and mechanical stability of the prepared surface at 75–125 mm/s

were compared. After considering all properties, Raman, cross-section microstructure, confocal laser scanning microscope, and Joule thermal analyses were performed on the 75 mm/s surface, and different effects of electric deicing were obtained while verifying that the surface was composed of micron-structured gully graphene. We explore a new simple, rapid, and repeatable method to prepare graphene surfaces with hydrophobic anti-icing and electrothermal deicing potentials on polymer substrates by microregulating the scanning speed based on a CO₂ laser.

It is worth noting that we employed the control variable method to systematically investigate the impact of scanning speed on the linewidth of the groove structure. Based on previous research methods, we first observed a significant linear negative correlation between scanning speed and the linewidth of the fabricated structure, which holds paramount importance for precise microregulation in laser manufacturing. Furthermore, we successfully achieved one-step fabrication of primitive continuous superhydrophobic graphene structures without relying on favorable factors, such as chemical modifications or bionic designs. The micron-structured graphene surfaces exhibited exceptional mechanical durability (contact angle change: -6.3° to $+7.2^{\circ}$ after 1000 bending cycles), stable icing delay (up 123.1%–161.5%), and an efficient electrical deicing effect (5 s inner defrosting, 90 s inner deicing, even more efficient). These results unequivocally demonstrate that CO₂ laser-induced graphene technology possesses remarkable characteristics for preparing hydrophobic, superhydrophobic, and electrothermal surfaces.

2. Materials and Methods

2.1. Information on Materials and Preparation Equipment

The materials include: polyimide film (thickness: 125 μm); deionized water (China, purchased from Jingdong Mall); copper foil (China, Stioo, CR-010S, purchased from Jingdong Mall); CO₂ laser (Synrad, Inc., Bedford, MA, USA, wavelength: 10.6 μm , pulse width: 100 ns, SYNRAD-p150), which produces LIG in ambient air atmosphere; ultrasonic cleaning machine (Shenzhen Chunlin Cleaning Equipment Co., Ltd, CR-010S, Shenzhen, China); and a constant-temperature drying box (Shaoxing Subo Instrument Co., Ltd, DHG-202, Shaoxing, China).

2.2. Characterization

The two-dimensional surface morphology and microstructure were observed by Focused ion beam-SEM (Thermo Fisher Scientific Inc., Thermo Scientific Helios 5 CX, Waltham, MA, USA), and an energy-dispersive X-ray spectroscopy (EDS) analysis was performed. Raman spectra were obtained using a confocal Raman spectrometer (Renishaw plc, Renishaw inVia, New Mills, UK) equipped with a 532-nm laser source. The confocal laser scanning microscope (CLSM, Keyence Corporation, VK-X1000, Higashi-Nakajima, Japan) was used to observe the surface morphology of the sample under a $\times 10$ lens. The contact angle was measured using a contact angle tester (Kruss Scientific Instruments Co., Ltd., DSA100, Mainz, Germany), and the results were tested three times. Repeated bending tests were performed with the motion controller (Beijing Micro nano optical instrument Co., Ltd., WNMC600, Beijing, China).

2.3. Preparation Process and Data Recording Method

First, the PI films were cleaned using an ultrasonic machine with distilled water and dried in a constant-temperature drying oven. Then, the laser beam was controlled using a digital oscillator, and the laser parameters were designed using the MarkingMate V2.7D-3.22 software. During the laser preparation process, the laser scanning speed, laser power, and laser pulse frequency were set to 50–125 mm/s (with an interval of 25 mm/s), 5.2 W, and 20 kHz, respectively. Afterward, the adjustment sample surface was located at the spot lens focus with a length of 95.5 mm, and the adjacent distance of the laser beam was 0.2 mm with a mode of row by row. With the other parameters fixed, the laser scanning speed was changed to study the effect on the surface morphology of graphene,

as shown in Figure 1. Finally, the delayed icing experiment was performed on a small refrigeration platform (DIY semiconductor refrigeration unit purchased from Alibaba Mall). The microscopic freezing state of the droplets was observed using a high-definition industrial camera (Kingsen Technology Co. Ltd., TDR 48MP FHD Camera V8, Dongguan, China) with a 180-X monocular optical microlens. A programmable DC power supply (RIGOL Technologies, Inc. DP800, Beijing, China) was used to provide a stable voltage. An infrared thermal imager (Fluke Corporation, TiX650, Everett, WA, USA) was used to observe and record the change in graphene surface temperature with time and the steady temperature under different voltages.

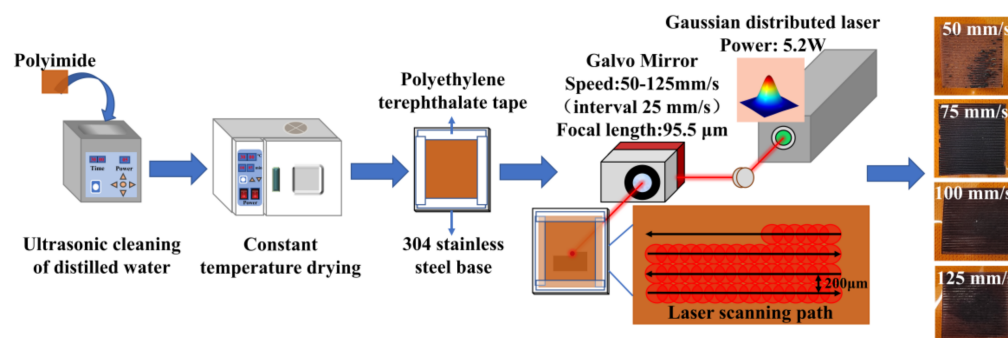


Figure 1. Process schematic to fabricate a micron-structure heatable graphene hydrophobic surface.

3. Results

3.1. Surface Morphology and Property Characterization

According to the SEM microstructure diagram in Figure 2a–d, parallel laser scanning tracks are arranged with a line spacing of 132–215 μm between adjacent tracks. Furthermore, the hydrophobic surface morphology varies with different scanning speeds. Specifically, the product falls off and is disarranged on the graphene surface at a scanning speed of 50 mm/s. Prolonged laser irradiation at this lower scanning speed causes the local excessive temperature on the PI surface, which results in excessive surface thermal stress and makes the product transition from an adhesion state to a bending state. In addition, small holes with dense distribution and large dispersed pores simultaneously appear on the surface of the product. These small holes indicate sufficient thermal decomposition on the PI film surface, while large holes result from insufficient thermal decomposition caused by a lack of direct contact between the PI film and laser layer. It takes a period of heat accumulation to generate a sufficient amount of gas to burst the bubble and form larger holes. However, at a scanning speed of 75 mm/s, the gaps between adjacent tracks on the hydrophobic surface are very small. The distribution of small holes is uniform and dense with an arc-shaped pattern that corresponds to the motion trajectory of the laser spot. Compared to a scanning speed of 50 mm/s, there is an increase in large hole density due to the insufficient thermal decomposition, since the PI film does not directly contact the laser layer. At a scanning speed of 100 mm/s, there is an observable gap between adjacent tracks on the hydrophobic surface. A sheet structure emerges with visible traces of small, circular holes, although their number decreases and sizes increase. For the graphene surface prepared at a scanning speed of 125 mm/s, an increase in gap between adjacent tracks and the emergence of discrete states were observed due to the higher laser scanning speed. The discrete state on the graphene surface was attributed to a decrease in the light spot overlap rate, which results from increasing the laser scanning speed and makes the edge shape of a scanning track to change from a straight line to a wavy shape. The dense porous structures on the product surface disappeared, and coexisting lamellar and fibrous structures were observed. This issue occurred because of a decrease in laser energy, which caused the insufficient thermal decomposition of the PI film and consequently inadequate gas release and exclusion. The adjustment made large bubbles burst and eventually formed explosive sheets and fibrous structures. Therefore, the samples prepared at a scanning speed of 75 mm/s were chosen

for the initial characterization, assessment of hydrophobic properties, and evaluation of the Joule thermal requirements based on the surface morphology of graphene.

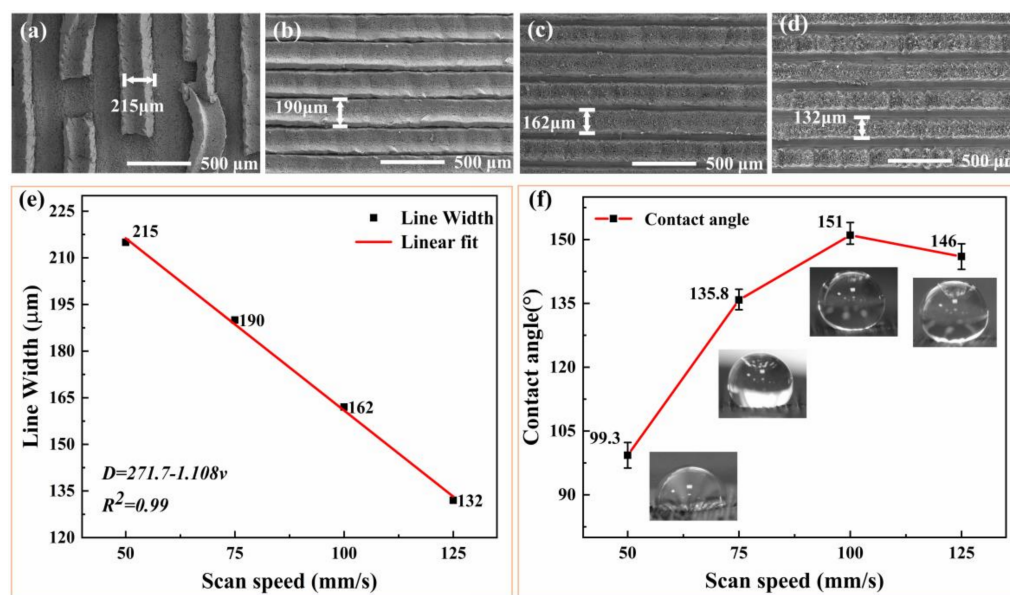


Figure 2. (a–d) Scanning electron microscope images of the prepared micron-level structures at 50 mm/s, 75 mm/s, 100 mm/s, and 125 mm/s laser scanning speed, scale bar: 500 μm; (e) Fit of the laser scanning speed versus the scan trajectory line width; (f) Contact angle characterization of the surfaces prepared with different scanning velocity parameters.

The basic SEM characterization results show that the graphene line widths varied under different scanning parameters. Figure 3c shows a scatter plot of the scan speed-line width and scanning velocity-line width, which indicates a negative correlation between scanning speed (v) and line width (D): $D = 271.7 - 1.108v$ ($R^2 = 0.99$). Figure 2d shows the contact angle data of micron-structure surfaces prepared at different scanning speeds. The surface prepared at a scanning speed of 50 mm/s was exactly identical to the SEM observation results. The water contact angle was only 99.3° due to the shedding of the micron graphene structure, but it has an improvement effect compared to the droplet state on the PI surface because the microgrooves remained after the graphene had been shed. The surface prepared at 75–125 mm/s exhibited hydrophobicity, and the surface prepared at 100 mm/s exhibited superhydrophobicity (CA = 151°). Corresponding to the SEM analysis, the laser scanning speed affects the line width and surface microstructure of the product, which exhibits different hydrophobic characteristics. According to the figure analysis, appropriately increasing the scanning speed is conducive to improving the surface hydrophobicity, but a scanning speed above a certain threshold will cause the opposite effect.

Based on the surface hydrophobicity of micron-structure gully graphene, the icing test was performed on the surface of a PI thin film. The PI film was placed on a semiconductor refrigeration platform, and the shape of liquid droplets on the PI film was carefully observed using a high-definition industrial camera. As shown in Figure 3a, the state of the liquid droplets in the PI film at room temperature is defined as $T = 0$ s. The droplet exhibited hydrophilicity on the PI surface; when the platform refrigeration switch was turned on, rapid cooling occurred at -23 °C. At $T = 14$ s, ice nuclei began to appear on the droplet on the PI film surface and gradually condensed from the bottom. At $T = 26$ s, the droplet completely froze and had an inverted elliptical cone shape. Subsequently, the same methodology was employed to investigate the icing process of droplets on the micron-structure gully graphene surfaces (75–125 mm/s). As shown in Figure 3b–d, at $T = 0$ s, the droplets exhibited a high contact angle (CA > 90°) on the surface. At $T = 26$ s, $T = 28$ s, and $T = 38$ s, ice nuclei emerged on the contact surface between droplets and graphene and gradually propagated upward from the bottom of the droplets until complete solidification

occurred at $T = 58$ s, $T = 57$ s, and $T = 68$ s, respectively. The overall morphology resembled that of a barrel cone. From the time perspective from when ice nuclei began to form to when the ice became completely frozen, there was an 85.7%–171.4% extension in the onset of ice nucleation and a 123.1%–161.5% delay in complete freezing. The micron-structure gully surface structure retained air within the gap between the droplet and surface, while air or other media trapped within the outer surface structure acted as a thermal resistance and impeded the energy transfer between the droplet and surface. The micron-structure graphene surface exhibits excellent hydrophobic properties and can effectively delay the occurrence of icing [52]. Therefore, it has great potential for application in anti-icing technology.

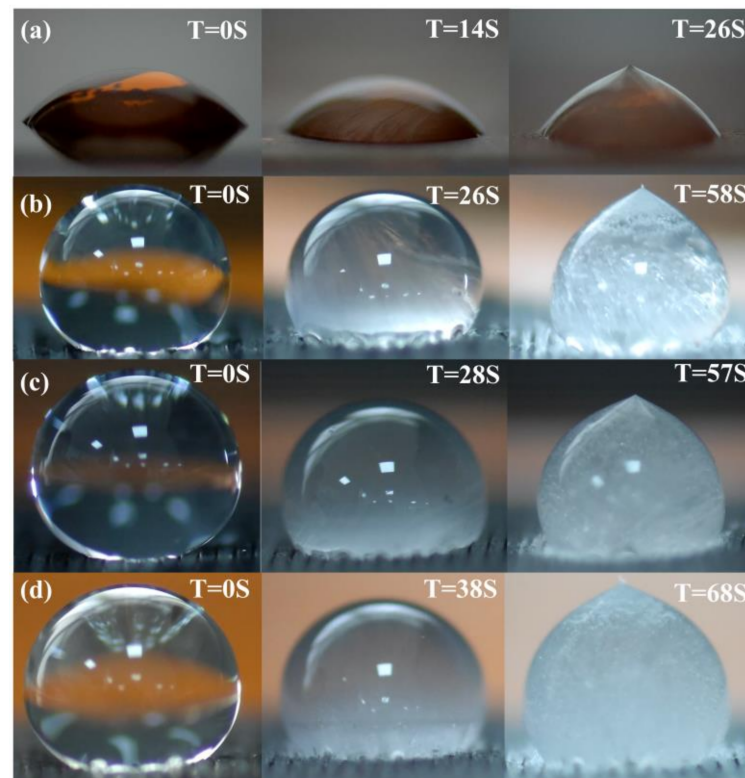


Figure 3. (a–d) Initial state, ice nuclei formation state, and complete icing state of water droplets on the PI films and surfaces prepared at scanning speeds of 75 mm/s, 100 mm/s, and 125 mm/s.

To verify the mechanical stability of the micron-structure gully graphene surface, the surface was subjected to 1000 cycles of mechanical cyclic bending with a bending radius of 1.5 cm, and the surface contact angle was tested every 200 cycles, as shown in Figure 4a. The surface prepared at 75 mm/s showed an unexpected increase in contact angle. The contact angle first significantly increased and subsequently decreased with the increase in the number of mechanical cycles. After 1000 bends, the overall contact angle increased by 7.2° . The contact angles of the surfaces prepared at 100 mm/s and 125 mm/s showed a decreasing trend, and they decreased by 3.4 – 6.5° after 1000 bending times. After the mechanical bending test, the cyclic icing and deicing performance of the prepared surface under the three parameters was tested. In Figure 4b–d, the data of complete icing and complete melting showed similar trends, the data of beginning icing and beginning melting showed similar changes, and all three surfaces showed a decrease in delayed icing performance during the five cycles. In particular, the delayed icing performance of the 75 mm/s, 100 mm/s, and 125 mm/s surfaces decreased by 19.2%, 14.5%, and 41.9%, respectively. Because there is water in the air, repeated icing and melting will make frost condense into water on the surface, which worsens the overall delayed icing effect. This part of the test was conducted after the data test in Figure 3. The first data in the cyclic icing and deicing test showed little change compared to the data in Figure 3, which indicate

that the delayed icing performance will recover to the original state when the surface is dry again. The two performance test results show that the trench graphene surface has mechanical stability and can be reused.

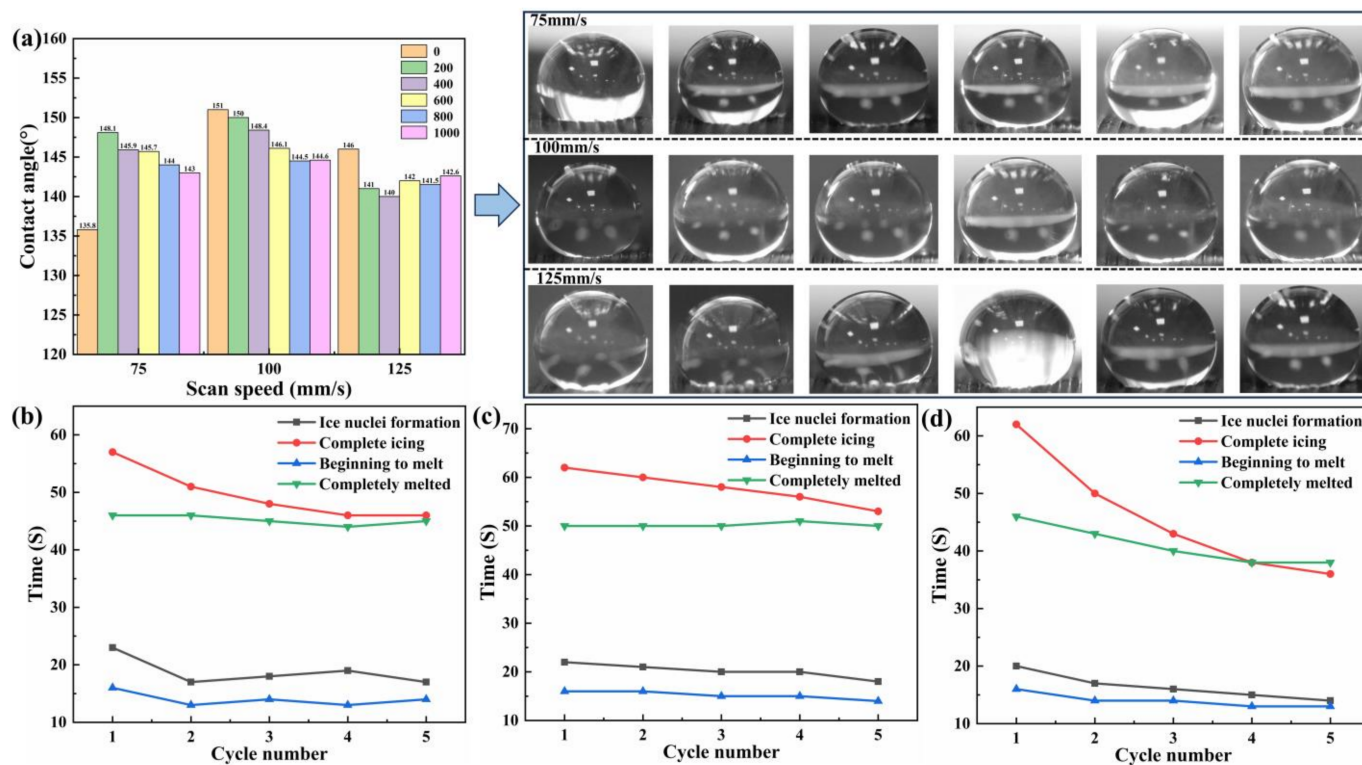


Figure 4. (a) Change in contact angle of the prepared surface with different scanning parameters after cyclic bending. Evaluation of the time to begin to freeze, completely freeze, begin to melt, and completely melt in the process of cyclic icing and melting for surfaces prepared at (b) 75 mm/s, (c) 100 mm/s, and (d) 125 mm/s.

3.2. Surface Morphology and Composition Characterization of the 75 mm/s Surface

According to the SEM analysis and hydrophobicity and mechanical stability analyses of the prepared surfaces at 75–125 mm/s in the previous section, the 75 mm/s sample showed a regular surface morphology, special hydrophobicity changes, a stable delayed icing effect, and fast melting efficiency in combination with the requirements of subsequent electric deicing. The composition, morphology, and Joule thermal properties of the surfaced prepared under these conditions were further tested. The distribution of elements on the hydrophobic surface prepared at a scanning speed of 75 mm/s was observed. The EDS test diagram in Figure 5a–c shows the distribution of C/N/O elements in the material. Figure 5a shows the surface test map of the scanning area, where there is a significant difference in C element density between scanning trajectory and gaps. However, the overall distribution is consistent with the SEM diagram. According to Figure 5b, the scanning area exhibited a significantly higher concentration of C element than that on the PI film, while N and O elements were present in lower concentrations. A distinct boundary line was formed by the distribution of elements at the scanning area and interface region of the PI surface. The EDS test diagram of the cross-section in Figure 5c shows a similar phenomenon to that in Figure 5b, which confirms that the original structure of PI was destroyed, photothermal effect will occur on the surface of polyimide film after laser irradiation, and C-H, C-O, C=O and C-N in the film will be broken and atoms will be rearranged, the O, N, and H atoms diffuse into the external environment in the form of a gas, and the C atoms combine to form a graphene structure during the laser irradiation on the surface of the PI thin film [20].

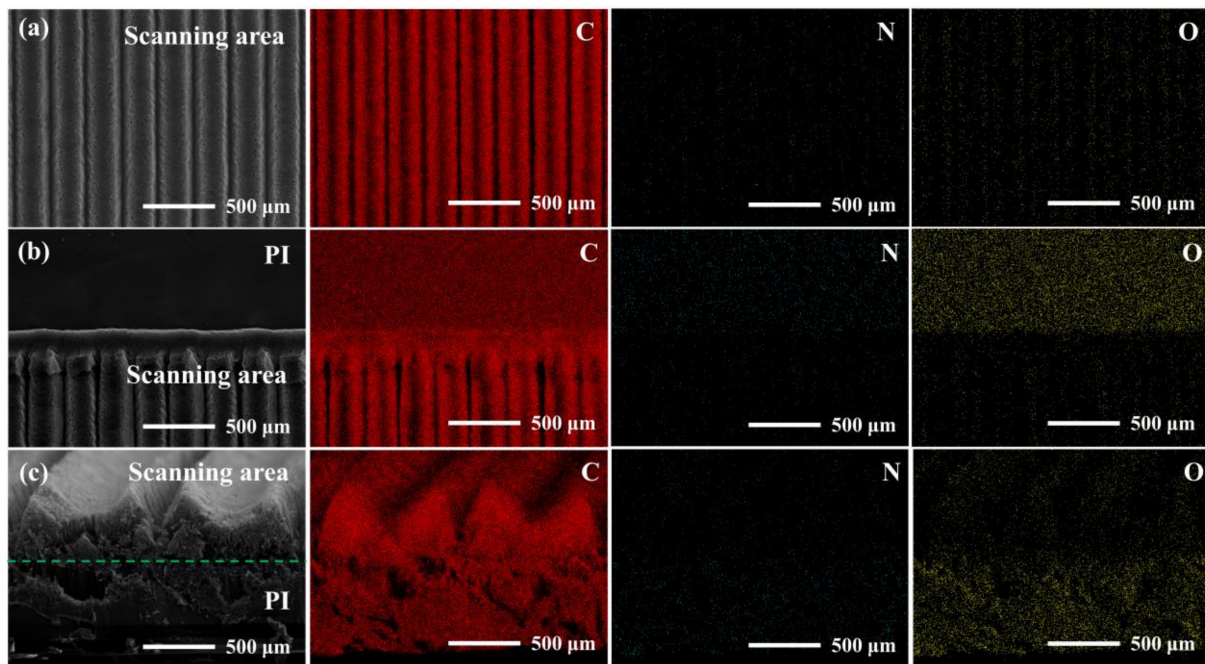


Figure 5. (a–c) EDS maps of C, N, and O elements at the surface, edges, and cross-sections of the surface prepared at a 75 mm/s scanning speed; scale bar: 500 μm .

To verify the presence of graphene in the laser scanning area, a Raman spectrum test was performed on both the PI thin film and the samples prepared at a scanning speed of 75 mm/s. As shown in Figure 6a, the Raman spectrum obtained from the laser scanning area exhibited three prominent carbon-related peaks, including peak D at 1344.26 cm^{-1} and peak G at 1582.77 cm^{-1} . The 2D peak was located at 2687.05 cm^{-1} , which indicates the generation of graphene on the laser-acted surface. The quantization of peak D, peak G, and the 2D peak ratio yielded $I_D/I_G = 1.3$ and $I_{2D}/I_G = 0.75$, respectively. A higher I_D/I_G value suggests more surface defects in graphene, which may be related to the uniform distribution of holes in Figure 2b or the high oxidation during preparation in an atmospheric environment [38]. In addition, the symmetrical 2D peak can be fitted to a single Lorentz curve with a center at 2687.05 cm^{-1} and a half-peak width of 47.5 cm^{-1} , which are typical features of highly ordered 2D graphite composed of randomly stacked graphene layers along the C-axis [53]. Overall, these characteristics confirm that the product is graphene and correspond to the results of SEM-observed pore defects. Figure 6b shows the cross-sectional view of the graphene structure obtained at a scanning speed of 75 mm/s. There are deep gullies between the tracks on the graphene surface, which confirms the conclusion drawn from SEM top-view observations of the gully surface. However, when the laser scanning trajectory plane approaches the center, there is a decrease in the graphene height because higher energy levels at the laser center with a Gaussian distribution cause similar etching effects on the graphene surface. According to Figure 6b, the height of the graphene was determined. The height was measured to be $110\text{ }\mu\text{m}$ at the edge of the gully in the graphene trajectory and $70\text{ }\mu\text{m}$ at the center of the trajectory. The bottom of the trajectory gap was successively connected. Laser confocal technology was used to enhance the depiction of micron-structure surface structures of graphene, which provided a refined two-dimensional height map and a three-dimensional map in Figure 6c to accurately quantify the surface topography. In the three-dimensional map, the height of the gully graphene trajectory was $110\text{--}147\text{ }\mu\text{m}$ at the edge and approximately $70\text{ }\mu\text{m}$ at the center. Additionally, uniformly distributed colors that represent different heights were observed on the graphene surface, which correspond with the SEM and cross-section analysis results. The roughness of the gully graphene surface was analyzed using Gwyddion-2.43, and the resulting Ra

value was 55.2 μm . A micron-structure gully graphene surface with higher roughness has better hydrophobicity [54].

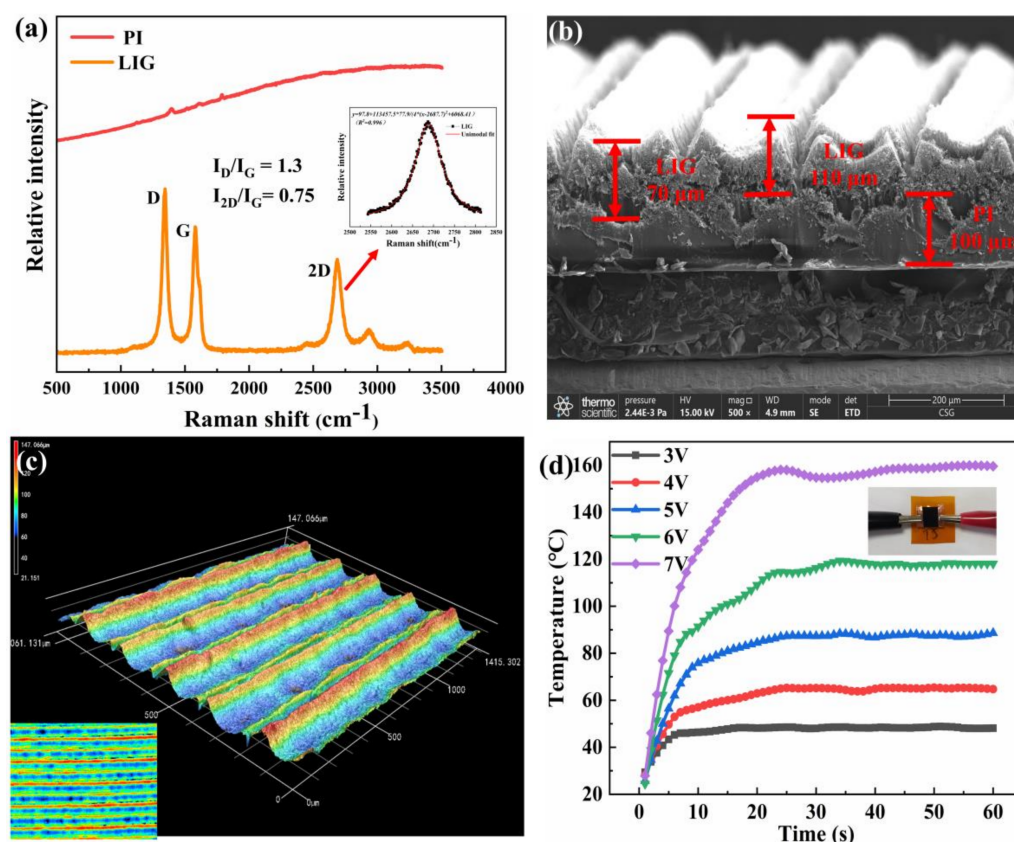


Figure 6. Results of surfaces prepared with laser scan parameters at 75 mm/s: (a) Raman spectra of PI films with the generated surfaces; (b) SEM images of the micron-structure graphene cross-sectional morphology; scale bar: 200 μm ; (c) CLSM images of the micron-structure graphene surfaces on PI substrates, $\times 10$; (d) Electrothermal connection mode and surface temperature-time variation curves of the micron-sized graphene surfaces at 3–7 V (interval: 1 V).

3.3. Thermal Deicing of the 75 mm/s Surface

Using the outstanding electrical conductivity and Joule thermal properties of graphene, fixed copper foils were attached to both sides of a rectangular graphene surface and connected to a DC power supply. Any form of carbon conductive region on the surface can be used to generate Joule heat. Then, the Joule thermal conditions of the graphene surface were investigated by regulating the power supply to maintain stable voltage values (3 V, 4 V, 5 V, 6 V, 7 V). According to the variation trend of graphene surface temperature in Figure 6d, the temperature rapidly increased within 20 s and subsequently gradually increased until reaching saturation. The steady-state temperature of the graphene surface can exceed 100 $^{\circ}\text{C}$ within 10 s under voltage levels of 6 V and 7 V, which indicates excellent electric heating performance. The surface can achieve precise temperature control at 3–5 V, and it exhibits excellent hydrophobicity and stable electric heating performance. It is expected to be widely applicable in various fields such as object surface deicing, microfluidics, and bacterial culture.

After the basic surface characteristic test and electric Joule thermal performance test, the deicing effect was tested. The surface was pasted on the semiconductor icing platform, and an HD camera was used to record the deicing effect. Figure 7 shows the test results. For the 4 V power supply, the frost in some areas could be melted within 20 s, and the ice could not be removed. With the 5 V power supply, the frost on the surface was melted within 5 s, and the completely frozen liquid droplets were melted into water droplets within 89 s.

The 6 V power supply voltage could quickly heat up the frost on the surface within 2 s and complete the ice melting within 60 s. The 7 V supply voltage enabled defrosting and deicing in 30 s. Thus, the surface can achieve precise temperature control at 3–7 V and exhibits excellent hydrophobicity, stable electric heating performance, and controllable defrosting and deicing performance.

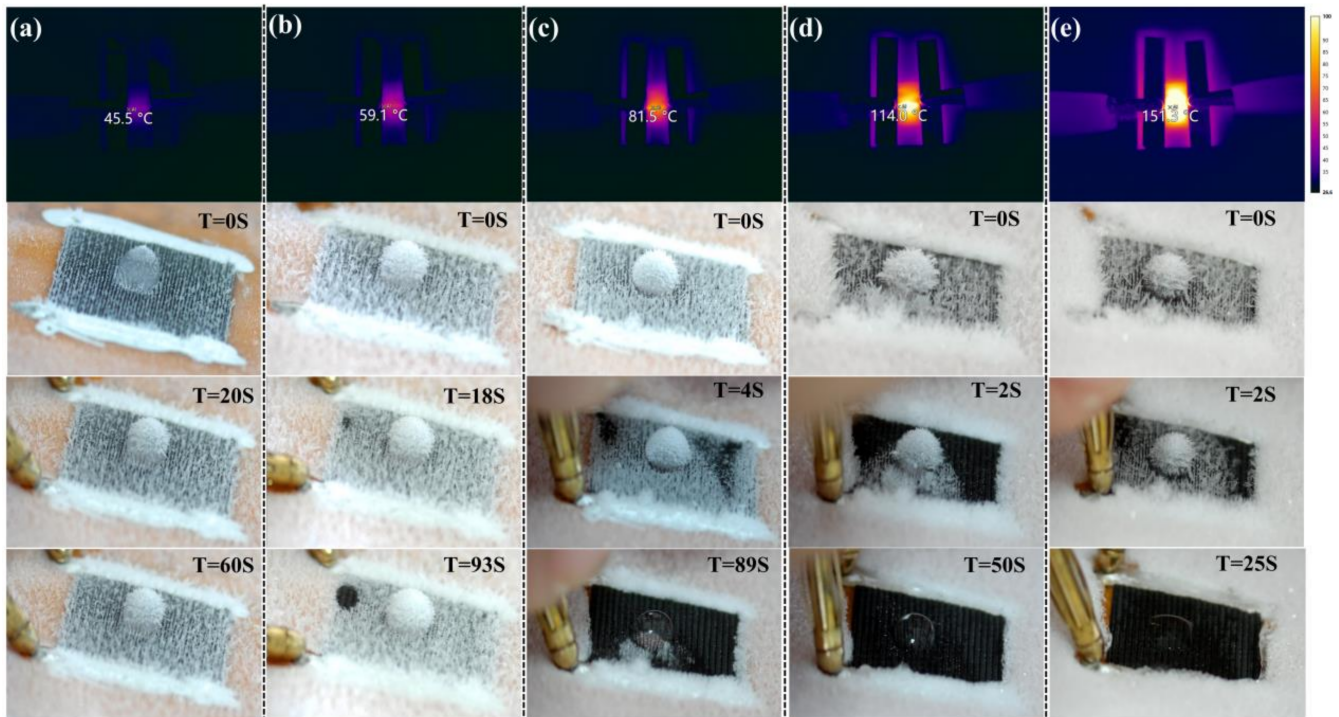


Figure 7. (a–e) Steady-state surface temperature and deicing effect for a 3–7 V voltage supply (1 V interval).

4. Conclusions

We utilized the 10.6 μm CO_2 laser direct writing technology to fabricate micron-structure gully and heatable hydrophobic graphene surfaces on PI substrates at different scanning speeds (50–125 mm/s). SEM images revealed that the graphene surface prepared at 50 mm/s exhibited a gully shape that appeared to fall off, and the graphene surfaces prepared at 75–125 mm/s had a furrow shape and a uniform distribution of microcoarse pore structures. Moreover, through linear fitting, we first observed a significant linear negative correlation between the linewidth of the fabricated structure and scanning speed. Additionally, we successfully achieved one-step fabricate of primitive continuous graphene structure with hydrophobic and superhydrophobic capability. The low-temperature icing test demonstrated that the delay time of ice nucleation on the surface of the graphene was 85.7%–171.4%, and the delay time for complete icing was 123.1%–161.5%. The mechanical property test shows that the graphene surface had mechanical stability and cyclic delay icing performance. The Raman and EDS spectral analysis of the surface prepared at 75 mm/s confirmed its identity as graphene, increase in the content of C elements on the surface with a decrease in the content of N elements, and O elements fit the formation mechanism of LIG. Additionally, the steady-state surface temperature of the sample increased from 45.5 $^{\circ}\text{C}$ to 151.3 $^{\circ}\text{C}$ when the applied voltage changed from 3 V to 7 V, which indicates excellent Joule thermal performance and the defrosting and deicing effect adjustment of the surface temperature through voltage control (5 s inner defrosting, 90 s inner deicing, even more efficient). In conclusion, the CO_2 laser-induced graphene technology can efficiently and quickly prepare micron-structure surfaces and convert polymer surfaces with hydrophilic wetting properties to those with hydrophobic wetting properties. These results prove that CO_2 laser-induced graphene technology possesses outstanding characteristics in the preparation of hydrophobic, superhydrophobic and electrothermal surfaces.

Author Contributions: Conceptualization, methodology, software, validation, data curation and writing—original draft preparation, S.L.; data curation, supervision writing—review and editing and funding acquisition, M.Z. and Q.H., validation, Y.Z., M.X. and X.L.; formal analysis, X.X.; investigation H.Z.; resources, Y.J. and C.Q.; visualization, project administration and funding acquisition, W.Q., M.L., C.Z. and C.Q. All authors have read and agreed to the published version of the manuscript.

Funding: The authors gratefully acknowledge the financial support from General Project of Sichuan General Aircraft Maintenance Engineering and Technology Research Center (GAMRC2021YB12), National key R&D program of Ministry of Science and Technology of China (2018YFC0809500), National Science Fund for Distinguished Young Scholars (52205238), Sichuan Science and Technology Program (2021YFG0249).

Institutional Review Board Statement: Not applicable.

Informed Consent Statement: Not applicable.

Data Availability Statement: Data sharing not applicable.

Conflicts of Interest: The authors declare no conflict of interest.

References

1. Song, Y.; Chen, L.; Yang, Q.; Liu, G.; Yu, Q.; Xie, X.; Chen, C.; Liu, J.; Chao, G.; Chen, X.; et al. Graphene-based flexible sensors for respiratory and airflow monitoring. *ACS Appl. Nano Mater.* **2023**, *6*, 8937–8944. [[CrossRef](#)]
2. Chhetry, A.; Sharifuzzaman, M.; Yoon, H.; Sharma, S.; Xuan, X.; Park, J.Y. MoS₂-decorated laser-induced graphene for a highly sensitive, hysteresis-free, and reliable piezoresistive strain sensor. *ACS Appl. Mater. Interfaces* **2019**, *11*, 22531–22542. [[CrossRef](#)] [[PubMed](#)]
3. Tamura, K.; Tang, C.; Ogiura, D.; Suwa, K.; Fukidome, H.; Takida, Y.; Minamide, H.; Suemitsu, T.; Otsuji, T.; Satou, A. Fast and sensitive terahertz detection with a current-driven epitaxial-graphene asymmetric dual-grating-gate field-effect transistor structure. *APL Photonics* **2022**, *7*, 126101. [[CrossRef](#)]
4. Ci, H.; Shi, Z.; Wang, M.; He, Y.; Sun, J. A review in rational design of graphene toward advanced Li-S batteries. *Nano Res. Energy* **2023**, *2*, e9120054. [[CrossRef](#)]
5. Zhang, Z.; Li, S.; Mi, B.; Wang, J.; Ding, J. Surface slip on rotating graphene membrane enables the temporal selectivity that breaks the permeability-selectivity trade-off. *Sci. Adv.* **2020**, *6*, eaba9471. [[CrossRef](#)]
6. Thakur, A.K.; Singh, S.P.; Kleinberg, M.N.; Gupta, A.; Arnusch, C.J. Laser-induced graphene–PVA composites as robust electrically conductive water treatment membranes. *ACS Appl. Mater. Interfaces* **2019**, *11*, 10914–10921. [[CrossRef](#)]
7. Moradi, S.A.H.; Ghobadi, N.; Zahrabi, F. Highly conductive supercapacitor based on laser-induced graphene and silver nanowires. *J. Mater. Sci. Mater. Electron.* **2022**, *33*, 18356–18363. [[CrossRef](#)]
8. Basu, A.; Roy, K.; Sharma, N.; Nandi, S.; Vaidhyanathan, R.; Rane, S.; Rode, C.V.; Ogale, S.B. CO₂ Laser direct written MOF-based metal-decorated and heteroatom-doped porous graphene for flexible all-solid-state microsupercapacitor with extremely high cycling stability. *ACS Appl. Mater. Interfaces* **2016**, *8*, 31841–31848. [[CrossRef](#)]
9. Xu, R.; She, M.; Liu, J.; Zhao, S.; Zhao, J.; Zhang, X.; Qu, L.; Tian, M. Skin-friendly and wearable iontronic touch panel for virtual-real handwriting interaction. *ACS Nano* **2023**, *17*, 8293–8302. [[CrossRef](#)]
10. Jayapiriya, U.S.; Rewatkar, P.; Goel, S. Miniaturized polymeric enzymatic biofuel cell with integrated microfluidic device and enhanced laser ablated bioelectrodes. *Int. J. Hydrog. Energy* **2020**, *46*, 3183–3192. [[CrossRef](#)]
11. Cheng, H.; Liu, J.; Zhao, Y.; Hu, C.; Zhang, Z.; Chen, N.; Jiang, L.; Qu, L. Graphene fibers with predetermined deformation as moisture-triggered actuators and robots. *Angew. Chem. Int. Ed.* **2013**, *52*, 10482–10486. [[CrossRef](#)] [[PubMed](#)]
12. Ling, Y.; Pang, W.; Li, X.; Goswami, S.; Xu, Z.; Stroman, D.; Liu, Y.; Fei, Q.; Xu, Y.; Zhao, P. Laser-induced graphene for electrothermally controlled, mechanically guided, 3d assembly and human-soft actuators interaction. *Adv. Mater.* **2020**, *32*, 1908475. [[CrossRef](#)]
13. Wang, W.; Han, B.; Zhang, Y.; Li, Q.; Zhang, Y.; Han, D.; Sun, H. Laser-induced graphene tapes as origami and stick-on labels for photothermal manipulation via marangoni effect. *Adv. Funct. Mater.* **2020**, *31*, 2006179. [[CrossRef](#)]
14. Zhang, D.; Yang, S.; Zhang, S.; Liu, W.; Pan, H.; Bai, X.; Ma, M.; Shang, Y.; Li, P. Epoxy resin/reduced graphene oxide composites with gradient concentration for aviation deicing. *ACS Appl. Eng. Mater.* **2023**, *1*, 1535–1542. [[CrossRef](#)]
15. Akhtar, N.; Anemone, G.; Farias, D.; Holst, B. Fluorinated graphene provides long lasting ice inhibition in high humidity. *Carbon* **2019**, *141*, 451–456. [[CrossRef](#)]
16. Novoselov, K.S.; Geim, A.K.; Morozov, S.V.; Jiang, D.E.; Zhang, Y.; Dubonos, S.V.; Grigorieva, I.V.; Firsov, A. Electric field effect in atomically thin carbon films supplementary. *Science* **2004**, *306*, 666–669. [[CrossRef](#)] [[PubMed](#)]
17. Kataria, S.; Wagner, S.; Ruhkopf, J.; Gahoi, A.; Pandey, H.; Bornemann, R.; Vaziri, S.; Smith, A.D.; Ostling, M.; Lemme, M.C. Chemical vapor deposited graphene: From synthesis to applications. *Phys. Status Solidi* **2014**, *211*, 2439–2449. [[CrossRef](#)]
18. Cambaz, Z.G.; Yushin, G.; Osswald, S.; Mochalin, V.; Gogotsi, Y. Noncatalytic synthesis of carbon nanotubes, graphene and graphite on SiC. *Carbon* **2008**, *46*, 841–849. [[CrossRef](#)]

19. Dreyer, D.R.; Park, S.; Bielawski, C.W.; Ruoff, R.S. The chemistry of graphene oxide. *Chem. Soc. Rev.* **2009**, *39*, 228–240. [[CrossRef](#)]
20. Lin, J.; Peng, Z.; Liu, Y.; Ruiz-Zepeda, F.; Ye, R.; Samuel, E.L.G.; Yacaman, M.J.; Yakobson, B.I.; Tour, J.M. Laser-induced porous graphene films from commercial polymers. *Nat. Commun.* **2014**, *5*, 5714. [[CrossRef](#)]
21. Dorin, B.; Parkinson, P.; Scully, P. Direct laser write process for 3D conductive carbon circuits in polyimide. *J. Mater. Chem. C* **2017**, *5*, 4923–4930. [[CrossRef](#)]
22. Cheng, C.; Wang, S.; Wu, J.; Yu, Y.; Li, R.; Eda, S.; Chen, J.; Feng, G.; Lawrie, B.J.; Hu, A. Bisphenol a sensors on polyimide fabricated by laser direct writing for onsite river water monitoring at attomolar concentration. *ACS Appl. Mater. Interfaces* **2016**, *8*, 17784–17792. [[CrossRef](#)] [[PubMed](#)]
23. Liu, H.; Zheng, Y.; Moon, K.-S.; Chen, Y.; Shi, D.; Chen, X.; Wong, C.-P. Ambient-air in situ fabrication of high-surface-area, superhydrophilic, and microporous few-layer activated graphene films by ultrafast ultraviolet laser for enhanced energy storage. *Nano Energy* **2021**, *94*, 106902. [[CrossRef](#)]
24. Chen, Y.; Long, J.; Xie, B.; Kuang, Y.; Chen, X.; Hou, M.; Gao, J.; Liu, H.; He, Y.; Wong, C.-P. One-step ultraviolet laser-induced fluorine-doped graphene achieving superhydrophobic properties and its application in deicing. *ACS Appl. Mater. Interfaces* **2022**, *14*, 4647–4655. [[CrossRef](#)] [[PubMed](#)]
25. Ye, R.; Chyan, Y.; Zhang, J.; Li, Y.; Han, X.; Kittrell, C.; Tour, J.M. Laser-induced graphene formation on wood. *Adv. Mater.* **2017**, *29*, 1702211. [[CrossRef](#)] [[PubMed](#)]
26. Chyan, Y.; Ye, R.; Li, Y.; Singh, S.P.; Arnusch, C.J.; Tour, J.M. Laser-induced graphene by multiple lasing: Toward electronics on cloth, paper, and food. *ACS Nano* **2018**, *12*, 2176–2183. [[CrossRef](#)] [[PubMed](#)]
27. Le, T.D.; Park, S.; An, J.; Lee, P.S.; Kim, Y. Ultrafast Laser Pulses Enable One-Step Graphene Patterning on Woods and Leaves for Green Electronics. *Adv. Funct. Mater.* **2019**, *29*, 1902771. [[CrossRef](#)]
28. Zhang, C.; Ping, J.; Ying, Y. Evaluation of trans-resveratrol level in grape wine using laser-induced porous graphene-based electrochemical sensor. *Sci. Total. Environ.* **2020**, *714*, 136687. [[CrossRef](#)]
29. Dixit, N.; Singh, S.P. Laser-induced graphene (LIG) as a smart and sustainable material to restrain pandemics and endemics: A perspective. *ACS Omega* **2022**, *7*, 5112–5130. [[CrossRef](#)]
30. Mahbub, H.; Saed, M.A.; Malmali, M. Pattern-dependent radio frequency heating of laser-induced graphene flexible heaters. *ACS Appl. Mater. Interfaces* **2023**, *15*, 18074–18086. [[CrossRef](#)]
31. Wang, W.; Lu, L.; Lu, X.; Liang, Z.; Tang, B.; Xie, Y. Laser-induced jigsaw-like graphene structure inspired by *Oxalis corniculata* Linn. leaf. *Bio Des. Manuf.* **2022**, *5*, 700–713. [[CrossRef](#)]
32. Zhang, J.; Xu, R.; Feng, J.; Xie, Y.; Zhou, T. Laser direct writing of flexible heaters on polymer substrates. *Ind. Eng. Chem. Res.* **2021**, *60*, 11161–11170. [[CrossRef](#)]
33. Wang, L.; Li, J.; Chen, Z.; Song, Z.; Meng, X.; Chen, X. Porous graphene-based photothermal superhydrophobic surface for robust anti-icing and efficient de-icing. *Adv. Mater. Interfaces* **2022**, *9*, 2201758. [[CrossRef](#)]
34. Peng, Y.; Zhao, W.; Ni, F.; Yu, W.; Liu, X. Forest-like laser-induced graphene film with ultrahigh solar energy utilization efficiency. *ACS Nano* **2021**, *15*, 19490–19502. [[CrossRef](#)] [[PubMed](#)]
35. Kan, Z.; Zhang, Q.; Ren, H.; Shen, M. Femtosecond laser induced formation of graphene nanostructures in water and their field emission properties. *Mater. Res. Express* **2019**, *6*, 085016. [[CrossRef](#)]
36. Kovalchuk, N.G.; Niherysh, K.A.; Felsharuk, A.V.; Svitlo, I.A.; Tamulevičius, T.; Tamulevičius, S.; Kargin, N.I.; Komissarov, I.V.; Prischepa, S.L. Direct patterning of nitrogen-doped chemical vapor deposited graphene-based microstructures for charge carrier measurements employing femtosecond laser ablation. *J. Phys. D Appl. Phys.* **2019**, *52*, 30LT01. [[CrossRef](#)]
37. Duy, L.X.; Peng, Z.; Li, Y.; Zhang, J.; Ji, Y.; Tour, J.M. Laser-induced graphene fibers. *Carbon* **2018**, *126*, 472–479. [[CrossRef](#)]
38. Ye, R.Q.; James, D.K.; Tour, J.M. Laser-induced graphene. *Acc. Chem. Res.* **2018**, *51*, 1609–1620.
39. Li, Y.; Luong, D.X.; Zhang, J.; Tarkunde, Y.R.; Kittrell, C.; Sargunraj, F.; Ji, Y.; Arnusch, C.J.; Tour, J.M. Laser-induced graphene in controlled atmospheres: From superhydrophilic to superhydrophobic surfaces. *Adv. Mater.* **2017**, *29*, 1700496. [[CrossRef](#)]
40. He, M.; Wang, G.; Zhu, Y.; Wang, Y.; Liu, F.; Luo, S. In-situ joule heating-triggered nanopores generation in laser-induced graphene papers for capacitive enhancement. *Carbon* **2021**, *186*, 215–226. [[CrossRef](#)]
41. Kim, K.Y.; Choi, H.; Van Tran, C.; Bin In, J. Simultaneous densification and nitrogen doping of laser-induced graphene by duplicated pyrolysis for supercapacitor applications. *J. Power Sources* **2019**, *441*, 227199. [[CrossRef](#)]
42. Liu, J.; Tang, J.; Gooding, J.J. Strategies for chemical modification of graphene and applications of chemically modified graphene. *J. Mater. Chem.* **2012**, *22*, 12435–12452. [[CrossRef](#)]
43. Tittle, C.M.; Yilman, D.; Pope, M.A.; Backhouse, C.J. Robust superhydrophobic laser-induced graphene for desalination applications. *Adv. Mater. Technol.* **2017**, *3*, 1700207. [[CrossRef](#)]
44. Lee, J.-U.; Lee, C.-W.; Cho, S.-C.; Shin, B.-S. Laser-induced graphene heater pad for de-icing. *Nanomaterials* **2021**, *11*, 3093. [[CrossRef](#)] [[PubMed](#)]
45. Nasser, J.; Lin, J.; Zhang, L.; Sodano, H.A. Laser induced graphene printing of spatially controlled super-hydrophobic/hydrophilic surfaces. *Carbon* **2020**, *162*, 570–578. [[CrossRef](#)]
46. Wu, W.; Liang, R.; Lu, L.; Wang, W.; Ran, X.; Yue, D. Preparation of superhydrophobic laser-induced graphene using taro leaf structure as templates. *Surf. Coat. Technol.* **2020**, *393*, 125744. [[CrossRef](#)]

47. Wang, Y.; Wang, G.; He, M.; Liu, F.; Han, M.; Tang, T.; Luo, S. Multifunctional laser-induced graphene papers with combined defocusing and grafting processes for patternable and continuously tunable wettability from superlyophilicity to superlyophobicity. *Small* **2021**, *17*, 2103322. [[CrossRef](#)]
48. Wang, J.; Zhang, Y.; He, Q. Stretchable superhydrophobic fluororubber fabricated by transferring mesh microstructures. *Soft Matter* **2023**, *19*, 1560–1568. [[CrossRef](#)]
49. He, Q.; Ma, Y.; Wang, X.; Jia, Y.; Li, K.; Li, A. Superhydrophobic flexible silicone rubber with stable performance, anti-icing, and multilevel rough structure. *ACS Appl. Polym. Mater.* **2023**, *5*, 4729–4737. [[CrossRef](#)]
50. Li, A.; Wei, Z.; Zhang, F.; He, Q. A high reliability super hydrophobic silicone rubber. *Colloids Surf. A Physicochem. Eng. Asp.* **2023**, *671*, 131639. [[CrossRef](#)]
51. He, Q.; Wang, J.; Wang, G.; Hao, X.; Li, A. Construction of a durable superhydrophobic flame-retardant coating on the PET fabrics. *Mater. Des.* **2023**, 112258. [[CrossRef](#)]
52. Wang, W.; Lu, L.; Li, Z.; Xie, Y. Laser induced 3D porous graphene dots: Bottom-up growth mechanism, multi-physics coupling effect and surface wettability. *Appl. Surf. Sci.* **2022**, *592*, 153242. [[CrossRef](#)]
53. Clerici, F.; Fontana, M.; Bianco, S.; Serrapede, M.; Perrucci, F.; Ferrero, S.; Tresso, E.; Lamberti, A. In situ MoS₂ decoration of laser-induced graphene as flexible supercapacitor electrodes. *ACS Appl. Mater. Interfaces* **2016**, *8*, 10459–10465. [[CrossRef](#)]
54. Alizadeh, A.; Yamada, M.; Li, R.; Shang, W.; Otta, S.; Zhong, S.; Ge, L.; Dhinojwala, A.; Conway, K.R.; Bahadur, V.; et al. Dynamics of ice nucleation on water repellent surfaces. *Langmuir* **2012**, *28*, 3180–3186. [[CrossRef](#)]

Disclaimer/Publisher’s Note: The statements, opinions and data contained in all publications are solely those of the individual author(s) and contributor(s) and not of MDPI and/or the editor(s). MDPI and/or the editor(s) disclaim responsibility for any injury to people or property resulting from any ideas, methods, instructions or products referred to in the content.